Organic Electronics 128 (2024) 107020

Contents lists available at ScienceDirect

Organic Electronics

journal homepage: www.elsevier.com/locate/orgel

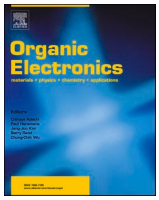

Confronting positions: *para- vs. meta*-functionalization in triindole for p-type air-stable OTFTs

Alba Cuadrado [a,b], Roger Bujaldón [a,b], Clara Fabregat [a,b], Joaquim Puigdollers [c], Dolores Velasco [a,b,*]

[a] Grup de Materials Orgànics, Departament de Química Inorgànica i Orgànica, Secció de Química Orgànica, Universitat de Barcelona, Martí i Franquès 1, E-08028, Barcelona, Spain
[b] Institut de Nanociència i Nanotecnologia (IN^{2}UB), E-08028, Barcelona, Spain
[c] Dept. Enginyeria Electrònica, Universitat Politècnica de Catalunya, Jordi Girona 1–3, E-08034, Barcelona, Spain

ARTICLE INFO

Keywords:
Organic electronics
OTFTs
p-type semiconductors
Triindole
Air-stable materials

ABSTRACT

The 5,10,15-trihexyl-10,15-dihydro-5*H*-diindolo[3,2-*a*:3′,2′-*c*]carbazole core, namely triindole, is well-known for its prominent hole-transporting properties and air stability. The functionalization of this core is also rather versatile, which allows the modulation of its properties by anchoring targeted scaffolds to different positions, e.g. 3,8,13 (*para* with respect to the nitrogens), 2,7,12 (analogously *meta*) or the nitrogen heteroatoms. Therefore, triindole excels as a pivotal semiconductor to be exploited in long-lasting organic thin-film transistors (OTFTs). This report aims to shed light on the effect of functionalizing whether *para* or *meta* positions with sulfurated moieties, in the pursuit of an enhanced performance in OTFTs. Remarkably, *meta*-substituted derivatives outshone their *para*- counterparts in terms of thermal, optical, intermolecular arrangement and semiconductor properties, claiming mobility values up to 2×10^{-3} cm^2 V^{-1} s^{-1} and a shelf lifetime beyond the analyzed period of 5 months. Analysis of the thin films by grazing incidence X-ray diffraction (GIRXD) and atomic force microscopy (AFM) revealed that the *meta*-substitution also induces a higher degree of order and better morphology, further corroborating the potential of this structural approach.

1. Introduction

Organic thin-film transistors (OTFTs), being one of the main basic components in next-generation electronics, are highly demanded in multiple routinely-used devices such as electronic paper, sensors and flat-panel displays [1–5]. The incorporation of organic semiconductors represents an advantageous strategy in front of the conventional silicon-based technology because they are light-weighted and permit the deposition of large and flexible surfaces at a lower energetic and economic cost [6–8]. The investigation of enhanced organic semiconductors is therefore of great interest for next-generation optoelectronic applications. Even though the cutting-edge organic materials have certainly outdone the performance of amorphous silicon, with charge mobility values beyond 10 cm^2 V^{-1} s^{-1} [9–11], most of them have yet to attain the air-stability and solubility required for a direct implementation into the market [12–14].

The assets of organic materials also include that intrinsic properties such as their energy levels or their intermolecular interactions can be easily adjusted by tailoring the molecular architecture. Considering that the semiconductor characteristics in organic electronics are closely related to the ease of injecting charges (determined by their energy levels) and their transport (governed by their intermolecular arrangement), the molecular design is a must-have step in any early-stage study. This encompasses the choice of both the nucleus and the functionalization patterning. 10,15-Dihydro-5*H*-diindolo[3,2-*a*:3′,2′-*c*]carbazole, commonly known as triindole, exemplifies the versatility of a hole-transporting core by excelling not only in OTFTs [15–19], but also in diverse applications such as organic light-emitting diodes (OLEDs) [20,21] and organic solar cells (OSCs) [22,23]. Indeed, this system exhibits strong π-π stacking interactions between adjacent molecules in the solid state, which together with the tendency to form highly ordered films, explains its prominent charge transport features [18,24,25]. In terms of optical properties, this nucleus inherits the bright emission of its structural building block, namely 9*H*-carbazole, but conveniently shifted to

* Corresponding author. Grup de Materials Orgànics, Departament de Química Inorgànica i Orgànica, Secció de Química Orgànica, Universitat de Barcelona, Martí i Franquès 1, E-08028, Barcelona, Spain.
E-mail address: dvelasco@ub.edu (D. Velasco).

https://doi.org/10.1016/j.orgel.2024.107020
Received 21 December 2023; Received in revised form 6 February 2024; Accepted 27 February 2024
Available online 28 February 2024

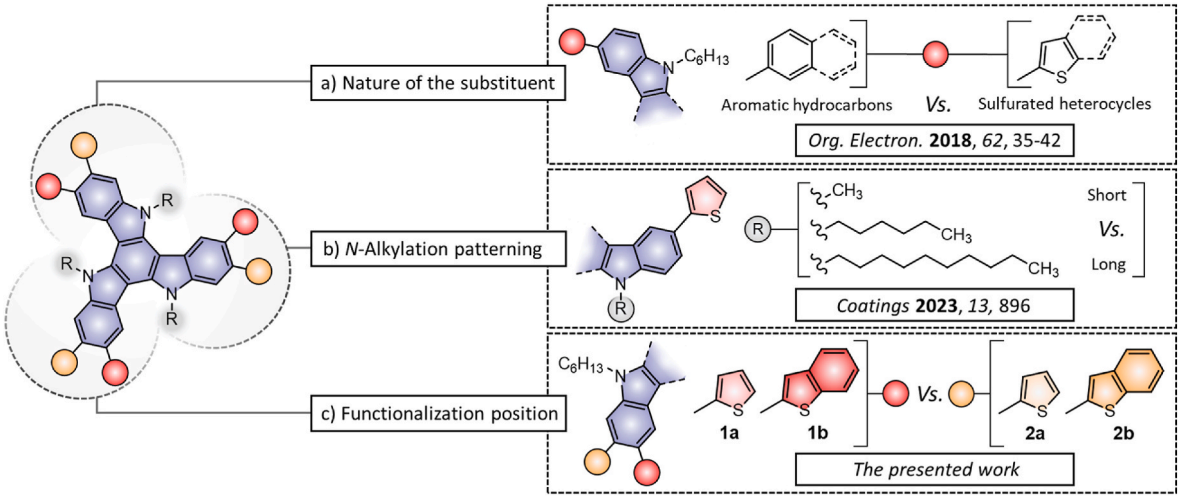

Fig. 1. Modification of the triindole core (in blue) based on different functionalization approaches of positions 3,8,13- (referred as *para*-, in red), 2,7,12- (referred as *meta*-, in orange) and the nitrogen heteroatoms (*N*-alkyl chains R-, in grey). These include the survey of: a) the nature of the substituents [26] and b) the length of the *N*-alkyl chains [27], as proposed in previous studies; c) the herein presented comparison between *para*- and *meta*-substitution patterns.

the blue region of the visible spectrum [17]. Another interesting point is that it possesses numerous positions that can be synthetically functionalized, enabling a varied palette of derived structures with fine-tuned characteristics. As depicted in Fig. 1, these functionalization points encompass three different kind of substitution motifs, which involve: positions 3,8,13 (referred as *para* with respect to the nitrogens), 2,7,12 (analogously denoted as *meta*) and the nitrogen heteroatoms. This topic has been explored in our research group, analyzing different structural modifications and functionalization patterns to optimize the semiconductor properties of the triindole core [26,27]. Fig. 1 reviews the antecedent contributions on this area along with the herein proposed study. As a first approach, we analyzed the influence of the aromatic substituents attached exclusively to *para* positions by comparing two different factors: the π-extension of the moieties, being one- or two-ringed, and their nature, being aromatic hydrocarbons or sulfurated heterocycles [26]. The presence of sulfur slightly ameliorated the charge carrier mobility, which goes in accordance with the relevance of sulfurated semiconductors in organic electronics [28–31]. Secondly, the length of the *N*-alkyl chains was studied in 10,15-dihydro-3,8,13-tris (5-methylthien-2-yl)-5*H*-diindolo[3,2-*a*:3′,2′-*c*]carbazole, which pointed out the relevance of medium-to-long alkyl chains over shorter ones in this particular system [27]. Albeit the aliphatic units exert a rather limited impact to the properties of the main core, they are decisive in determining the arrangement and morphology in the solid state. Finally, the aim of the present study is the comparison between *para*- and *meta*-substitution of sulfurated heterocyclic scaffolds in 5,10,15-trihexyl-10,15-dihydro-5*H*-diindolo[3,2-*a*:3′,2′-*c*]carbazole, a change that is prone to directly affecting the degree of conjugation throughout the π-system and the intermolecular interactions in the solid state. Further insight will be acquired by means of the single-crystal structures and X-ray diffraction patterns of the films. The interest in the triindole core also resides on the notoriously long lifetime periods it displays as the active layer of a device [17,18,26,27], claiming a highly sought-after feature that is often hastily monitored in the existing literature. Therefore, this factor is likewise analyzed in this work.

2. Experimental section

2.1. Instrumentation and methods

The synthetic procedure and characterization is compiled in the Supporting Information. ^{1}H NMR spectra were acquired in a Varian Mercury instrument (400 MHz) and ^{13}C NMR in a Bruker 400 MHz Advance III spectrometer (100 MHz). NMR spectra were processed using the MestRec Nova software (version 14.2.0) and referenced using the solvent signal. The single crystal structure was examined with a D8 Venture System equipped with a multilayer monochromator and a Mo microfocus (λ = 0.71073 Å). The frames were integrated with the Bruker SAINT software package via a narrow-frame algorithm. The structure was elucidated and refined using the Bruker SHELXTL software package. Thermogravimetric analyses (TGA) and differential scanning calorimetry (DSC) thermograms were recorded at a scan rate of 10 °C min^{-1} under nitrogen atmosphere in a TA Instruments Q50 and TA Instruments Q2000 calorimeter, respectively. Absorption and emission spectra were recorded at room temperature in a Varian Cary UV–Vis–NIR 500E spectrophotometer and a PTI 810 fluorimeter, respectively. Fluorescence quantum yields (Φ_f) were determined by means of an integrating sphere both in solution and in the solid state. Thin films for absorption and emission measurements were deposited over quartz substrates by thermal vacuum evaporation (below 10^{-6} mbar). Cyclic voltammograms were collected at 100 mV s^{-1} under quiescent conditions and under argon atmosphere employing a cylindrical three-electrode cell connected to a microcomputer-controlled potentiostat/galvanostat Autolab with PGSTAT30 equipment and GPES software (version 4.9). The reference was an Ag/Ag^{+} electrode (10^{-3} M $AgNO_3$ in acetonitrile), the working electrode consisted of a glassy-carbon electrode and the counter electrode was a platinum wire. All compounds were dissolved in distilled dichloromethane (10^{-3} M) along with tetrabutylammonium hexafluorophosphate (TBAP, 0.1 M) as the supporting electrolyte. All potentials were referred to the Fc^{+}/Fc redox couple. The ionization potentials (IP) were extracted from the onset of the first oxidation peak ($^{ox}E_{onset}$) as IP = $^{ox}E_{onset}$ + 5.39, where 5.39 eV corresponds to the formal potential in the Fermi scale of the Fc^{+}/Fc couple [32]. The electron affinities (EA) were estimated as EA = IP − $^{opt}E_{gap}$, in which the optical gap energies ($^{opt}E_{gap}$) were calculated from the $\lambda_{abs,onset}$ of the absorption spectra in CH_2Cl_2. The IP values in the solid state were determined under aerated conditions by the photoelectron emission method [33], employing vacuum-evaporated thin-films (10^{-6} mbar) of the synthesized compounds deposited over fluorine-doped SnO_2-coated glass substrates. The photoelectron emission spectra were acquired by applying a negative voltage of 300 V to the sample substrate whilst it was irradiated with a monochromatic beam. The photocurrent measurements were conducted with a 6517B Keithley electrometer connected to the counter electrode. The monochromatic light source was generated with a deep UV deuterium light source ASBN-D130-CM and CM110 1/8 m monochromator. Out-of-plane grazing incidence X-Ray

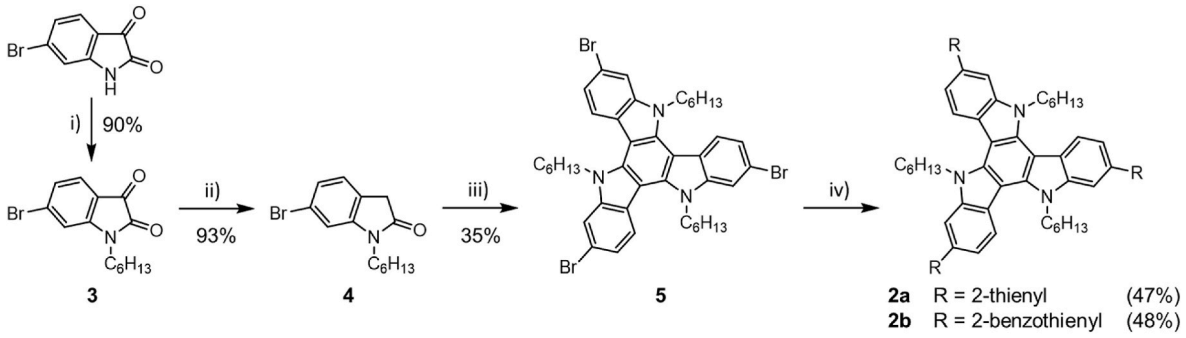

Scheme 1. Synthetic route towards the *meta*-substituted compounds **2a**−**b**.
Reagents and conditions: i) K_2CO_3, $C_6H_{13}Br$, DMF, RT; ii) $NH_2NH_2{\cdot}H_2O$, reflux; iii) $POCl_3$, reflux; iv) 2-thienylboronic acid (**2a**) or 2-benzothienylboronic acid (**2b**), $Pd(PPh_3)_4$, K_2CO_3, THF:H_2O (6:1 v/v), reflux.

diffraction (GIXRD) measurements of the thin-films (75 nm thickness) were acquired in a PANalytical X'Pert PRO MRD diffractometer in an optimized angle of incidence around 0.18°. It incorporated a PIXcel detector, a parabolic Göbel mirror at the incident beam and a parallel plate collimator at the diffracted beam, with Cu Kα radiation (λ = 1.5418 Å) and a work power of 45 kV × 40 mA. The morphology of the layers, studied by atomic force microscopy (AFM), was analyzed using an AFM Dimension 3100 system connected to a Nanoscope IVa electronics unit (Bruker).

2.2. OTFT fabrication and characterization

OTFT devices were fabricated in a bottom-gate top-contact geometry. The substrates consisted of thermally-oxidized crystalline Si/SiO_2 wafers with a SiO_2 thickness of ca. 115 nm. The gate side of the silicon wafer was partially treated with ammonium fluoride. The substrates were then cleaned by subsequent ultrasonic treatments in acetone, isopropanol and water, dried using a nitrogen blow and heated at 100 °C for 5 min. The SiO_2 surface was functionalized with octadecyltrichlorosilane (OTS) as self-assembled monolayer (SAM) [34] by immersing the substrates in a solution of OTS (2 mM) in toluene for 24 h at room temperature. Then, the substrates were cleansed by subsequent ultrasonic treatments in toluene, acetone and isopropanol, and eventually dried using a nitrogen blow and heated at 100 °C for 5 min. The organic compounds were deposited by thermal evaporation under vacuum (pressure below 10^{-6} mbar). The sublimation temperature was manually controlled for each compound to maintain a deposition rate of 0.3 Å s^{-1} until a thickness of 75 nm was achieved. The wafers were then transferred to another vacuum system to deposit the gold contacts. The drain and source electrodes were defined by a shadow mask, providing a channel length and width of 80 μm and 2 mm, respectively. The OTFTs were characterized under ambient conditions in the dark. The electrical characteristics were recorded employing a Keithley 2636A source meter. The charge carrier mobility was calculated in the saturation regime (μ_{sat})

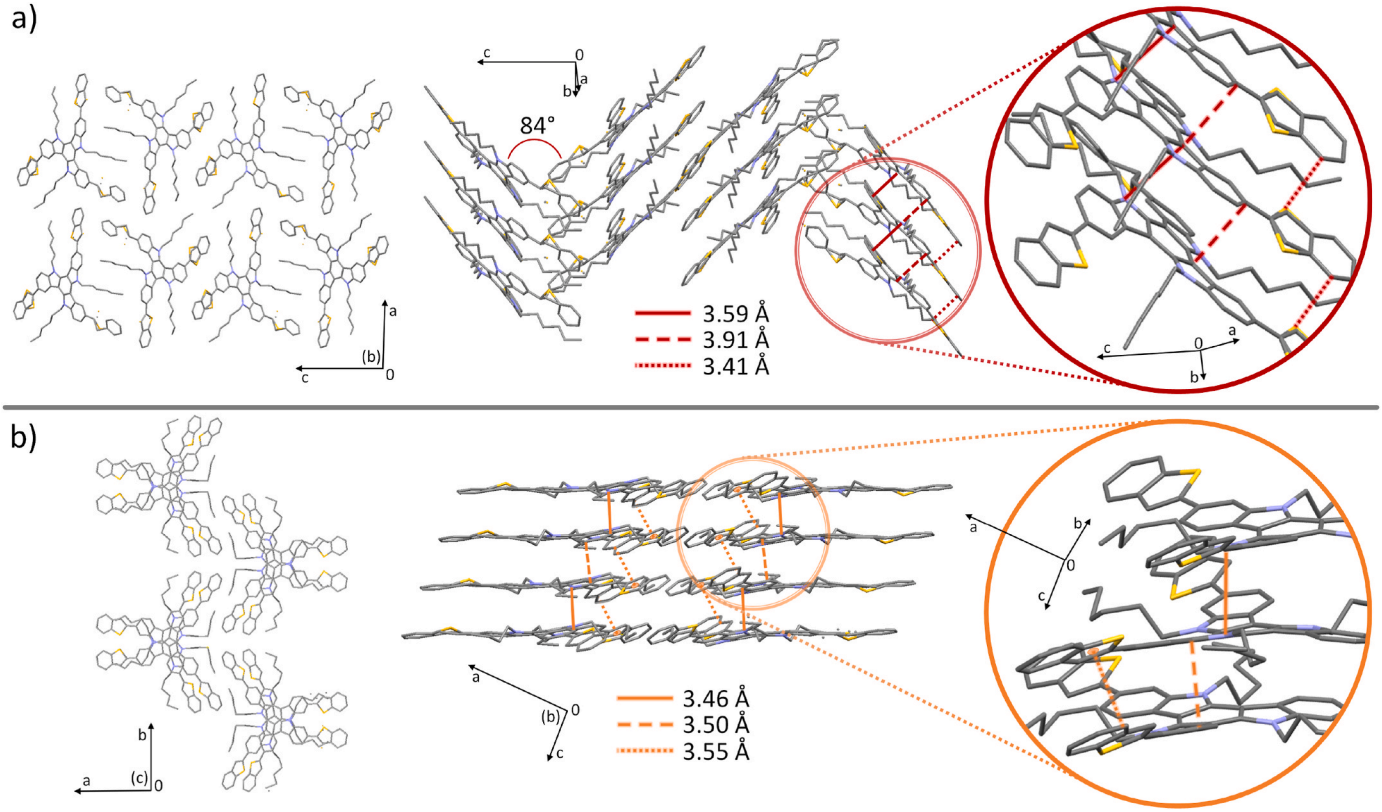

Fig. 2. Different projections of the crystal structures and the shortest π-π distances of compounds: a) **1b** and b) **2b**. Hydrogen atoms have been omitted for clarity.

Table 1
Thermal, photophysical and electrochemical properties of compounds **1a**,**b** and **2a**,**b**.

	T_d[a] (°C)	T_m[b] (°C)	T_c[b] (°C)	Φ_f[c]	$^{opt}E_{gap}$[d] (eV)	$^{ox}E_{onset}$[e] (V)	IP[f] (eV)	EA[g] (eV)	IP_{film}[h] (eV)
1a	433	166	106	0.15 (0.03)	3.22	0.21	5.6	2.4	5.11
1b	435	217	180	0.36 (0.04)	3.13	0.29	5.7	2.6	5.12
2a	410	233	224	0.36 (0.04)	3.06	0.18	5.6	2.5	5.12
2b	450	279	252	0.49 (0.05)	2.94	0.18	5.6	2.7	5.11

[a] Onset decomposition temperatures (T_d).
[b] Melting (T_m) and crystallization (T_c) temperatures.
[c] Absolute fluorescence quantum yields (Φ_f) measured in CH_2Cl_2 with an integrating sphere (λ_{exc} = 330 nm). The values in parenthesis correspond to the Φ_f in the solid state, acquired analogously from vacuum-deposited films over quartz.
[d] Optical energy gaps ($^{opt}E_{gap}$) estimated from the absorption spectrum ($\lambda_{abs,onset}$).
[e] Onset oxidation potentials *vs.* Fc^+/Fc ($^{ox}E_{onset}$) estimated from cyclic voltammetry of a 1 mM solution of the compound in CH_2Cl_2.
[f] Ionization potentials estimated as IP = $^{ox}E_{onset}$ + 5.39.
[g] Electron affinities estimated as EA = IP – $^{opt}E_{gap}$.
[h] Ionization potentials in film (IP_{film}), extracted from the photoelectron emission spectra.

from Equation (1):

$$I_D = \mu_{sat} C_{ox} \frac{W}{2L} (V_G - V_{th})^2 \quad (1)$$

where W and L correspond to the channel width and length, respectively, and C_{ox} is the capacitance per unit area of the gate insulator. All devices were stored under ambient conditions in the dark.

3. Results and discussion

3.1. Synthesis

Scheme 1 compiles the synthesis of the *meta*-substituted triindoles **2a**,**b**. Compounds **1a** [27] and **1b** [26] have been synthesized analogously, as described in the literature. Commercially available 6-bromoisatin was *N*-alkylated to compound **3** with 1-bromohexane in anhydrous DMF, using K_2CO_3 as base. The subsequent Wolff-Kishner reduction [35] afforded oxindole **4** in an excellent yield. The tribrominated precursor **5** was then achieved through a cyclocondensation reaction using $POCl_3$. Finally, the Suzuki-Miyaura cross-coupling reaction [36] of **5** and either 2-thienyl or 2-benzothienyl boronic acids successfully yielded the desired products **2a** and **2b**, respectively.

3.2. Crystallographic data

Single crystal structures of organic materials are key to unravel the main intermolecular interactions and the resultant molecular packing. In this study, we could conveniently elucidate the single crystal structure of the *meta*-substituted 2-benzothienyl derivative **2b**, which crystallized as light-yellow needles from the slow evaporation of a dichloromethane and ethanol mixture. The crystal could be ascribed to a space group $P2_1/c$ of the monoclinic system, with unit cell dimensions of a = 27.470(4) Å, b = 22.830(3) Å, c = 8.2247(10) Å, β = 93.174(5)° and volume = 5150.1 (12) $Å^3$ (Table S1). The single crystal structure of compound **2b** is depicted in Fig. 2 alongside that of the *para* counterpart **1b** [26] for comparison.

The main difference between both structures is the type of packing. The *para*-substituted **1b** exhibits slightly displaced face-to-face π-stacked columns that are connected to each other through edge-to-edge interactions, which could be associated to a γ packing [37,38]. Contrastingly, the *meta*-substituted **2b** preserves the β-type packing, also known as sheet-like, of the unsubstituted triindole nucleus, which is characterized by strong π-π interactions and low contribution from edge-to-face π···C–H contacts. In terms of charge transport, the γ-type packing could be considered favorable because it allows a more versatile 2D charge transport through face-to-face and edge-to-face π-π interactions, meaning that is less susceptible to localized traps or structural defects [39]. Nevertheless, the columnar arrangement of the β-type packing is generally acknowledged as the most optimal one due to the closest and steadiest π-stacking [38–40]. Regarding the π-π distances, the packing regime of **2b** exhibits a slipped face-to-face disposition along the b-axis with favorably short interplanar distances of 3.46 and 3.50 Å. In fact, these values ameliorate the π-π distances exhibited by the unsubstituted analog [18]. The triindole nucleus of **1b** slightly deviates from planarity, so the direct π-π interactions along the c-axis vary from 3.59 to almost 4 Å depending on the contact region (Fig. 2a). Intramolecularly, the benzothienyl scaffolds in **2b** show just a slight deviation from planarity with respect to the triindole nucleus, with dihedral angles from 9.3 to 16.0° that are similar to those observed in **1b**. However, **2b** presents free rotation in one of the benzothienyl moieties, which causes a minor disorder in positions S2/C34. This disorder and the dihedral angles are specified in the ORTEP projection (Fig. S1). The closest distances between benzothienyl rings are slightly lower in the case of **1b**, with values of 3.41 Å in front of the 3.55 Å of **2b**.

3.3. Physical characterization

The physical characterization of derivatives **1a**,**b** and **2a**,**b**, comprising the main thermal, optical and electrochemical properties, is compiled in Table 1. The thermogravimetric analysis revealed remarkably good thermal stabilities for all derivatives, with onset decomposition temperatures (T_d) above 400 °C under nitrogen atmosphere (Fig. S2), making them suitable for the vacuum-deposition process. The differential scanning calorimetry curves (Fig. S3) confirmed their crystalline nature, displaying sharp endothermic peaks for the melting courses (T_m) well above the room temperature, and the exothermic counterparts corresponding to the crystallization processes (T_c). Notably, the *meta*-substituted derivatives show much higher T_m values than their *para* analogs.

The absorption and emission spectra of this series of compounds, recorded in a dichloromethane solution (10 μM) and in the solid state, are represented in Fig. S4. The maximum absorption and emission peaks, and the $\lambda_{abs,onset}$ values are collected in Table S2. The introduction of sulfurated moieties in *meta* positions derives into a higher bathochromic shift of the maximum absorption than in *para*, both in solution and in the solid state. The onset wavelengths of the least energetic absorption bands in solution, which are typically used to estimate the optical energy gaps ($^{opt}E_{gap}$), follow the same tendency. Consequently, the *meta*-substituted derivatives display lower $^{opt}E_{gap}$ than the *para*-substituted ones, which is indicative that the formers permit a higher π-conjugation between the main core and the sulfurated moieties. The red-shift observed in the absorption and emission spectra from solution to the solid state, associated to aggregation, is again more pronounced in the *meta*-substituted derivatives **2a**,**b** ($\lambda_{em,max}$ shifts of 36 and 62 nm, respectively). Contrarily, derivatives **1a**,**b** only exhibit a shift of 8–11 nm from this step. In terms of emission, derivatives **2a**,**b** also outshine their analogs with higher Φ_f values in solution, in which **2b** features the highest amongst all the studied compounds with a value of

Table 2
OTFTs characteristics of devices based on compounds **1a**,**b** and **2a**,**b**.

	$\mu_{h,max}$ [a] ($cm^2\ V^{-1}\ s^{-1}$)	$\mu_{h,av}$ [b] ($cm^2\ V^{-1}\ s^{-1}$)	V_{th} [b] (V)	I_{on}/I_{off} [c]
1a	2.3×10^{-4} (1.3×10^{-4})	$(2.0 \pm 0.3) \times 10^{-4}$	$+6 \pm 4$	$\sim 10^4$
1b	4.4×10^{-4} (4.2×10^{-4})	$(4.0 \pm 0.3) \times 10^{-4}$	-7 ± 3	$\sim 10^4$
2a	1.0×10^{-3} (7.0×10^{-4})	$(9.2 \pm 0.9) \times 10^{-4}$	$+4 \pm 3$	$\sim 10^5$
2b	2.0×10^{-3} (1.6×10^{-3})	$(1.9 \pm 0.2) \times 10^{-3}$	-7 ± 2	$\sim 10^5$

[a] Maximum hole mobility value ($\mu_{h,max}$) registered for a single device on the first 3 days after fabrication. The values in parenthesis correspond to the mobility of the same device registered after ca. 5 months.

[b] Average mobility ($\mu_{h,av}$) and threshold voltage (V_{th}) values calculated from 8 analogous devices.

[c] Maximum I_{on}/I_{off} ratio.

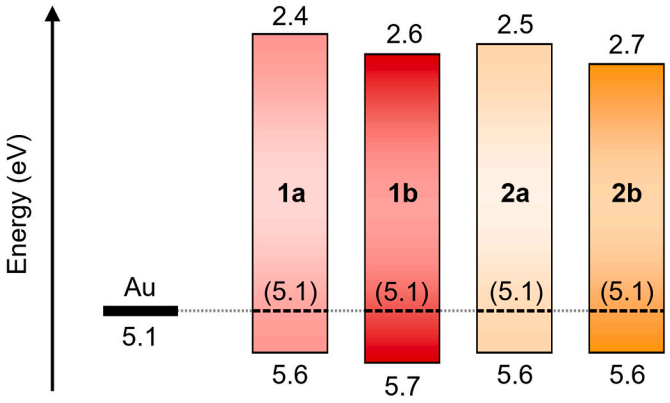

Fig. 3. Energy levels of the functionalized-triindole derivatives **1a**,**b** and **2a**,**b** with respect to the gold work function. The ionization potentials determined in the solid state are also indicated (dashed lines), with their values in parenthesis.

0.49. However, all Φ_f values drop to 0.05 or below in the solid state, which is typically associated to aggregation-caused quenching.

The electrochemical properties were investigated by cyclic voltammetry in dichloromethane (Table 1 and Fig. S5). All compounds show more than one oxidation process, being the first one quasi-reversible, whereas no reduction process was observed. Compounds **1b** and **2b** point to additional oxidation processes, presumably derived from the incorporation of the 2-benzothienyl scaffolds. The ionization potential values were dually estimated: from the onset oxidation potentials of the first oxidation steps in solution, and by the photoelectron emission technique in vacuum-evaporated thin-films (Fig. S6). All triindole derivatives showed similar ionization potentials, especially through photoelectron emission in the solid state (ca. 5.1 eV). Considering that the gold work function is analogously 5.1 eV, all compounds exhibit excellent IP values to allow the hole injection and transport. Moreover, their energy levels are sufficiently low-lying (below 4.9 eV) to grant

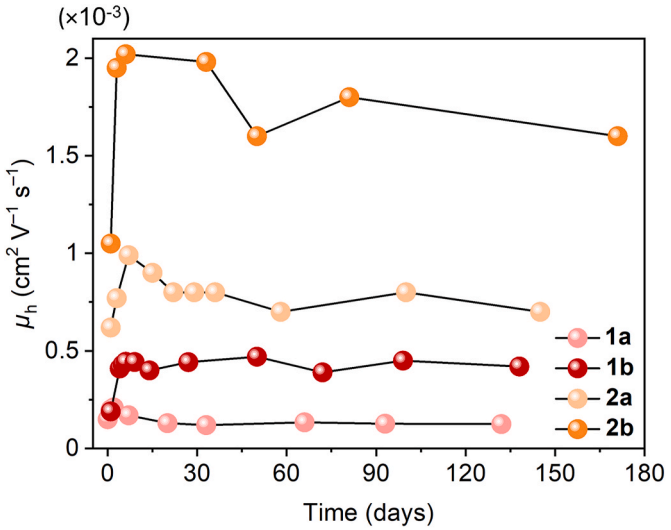

Fig. 5. Evolution of the μ_h of a representative device of each derivative throughout a period of ca. 5 months.

stability against atmospheric oxygen [7], which is essential to provide durable devices under ambient conditions. The energy diagrams together with the gold work function are represented in Fig. 3.

3.4. Organic thin-film transistors

Charge transport properties of the synthesized triindole derivatives were studied as the organic active layer of bottom-gate top-contact OTFTs. The organic materials were vacuum-deposited over Si/SiO_2 substrates functionalized with an octadecyltrichlorosilane (OTS) monolayer. The gold drain and the source electrodes were deposited on top of the organic layer by vacuum thermal evaporation using a shadow mask, which defines the dimensions of the final devices. Table 2 compiles the main characteristics of the devices. All derivatives present p-type field-effect behavior with a slight deviation from ideality, as revealed by the kinks between high and low V_G regions in the saturation regime (Fig. 4). This phenomenon, which is commonly observed in OTFT devices, could have diverse microscopic origins [41,42]. As suggested in the literature, the OTFT characteristics were extracted from the slope corresponding to the high V_G region.

Interestingly, the OTFTs based on *meta*-substituted triindoles **2a**,**b** clearly outperformed their *para* analogs **1a**,**b** in terms of both the charge mobility and I_{on}/I_{off} ratio. For instance, **2b** exhibited the highest hole mobility with a value of 2×10^{-3} $cm^2\ V^{-1}\ s^{-1}$, which represents one order of magnitude higher than its *para*-substituted counterpart **1b**. The output characteristics of these devices are displayed in Fig. S7 of the Supporting Information. In a lower degree, the π-extension of the

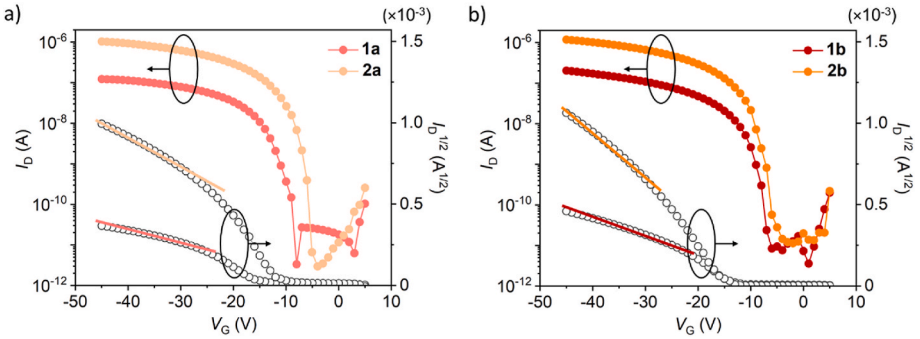

Fig. 4. Transfer ($V_D = -40$ V) and saturation characteristics of representative OTS-functionalized OTFT devices fabricated with compounds: a) **1a** and **2a**; b) **1b** and **2b**. The depicted measures were acquired 1–3 days after fabrication.

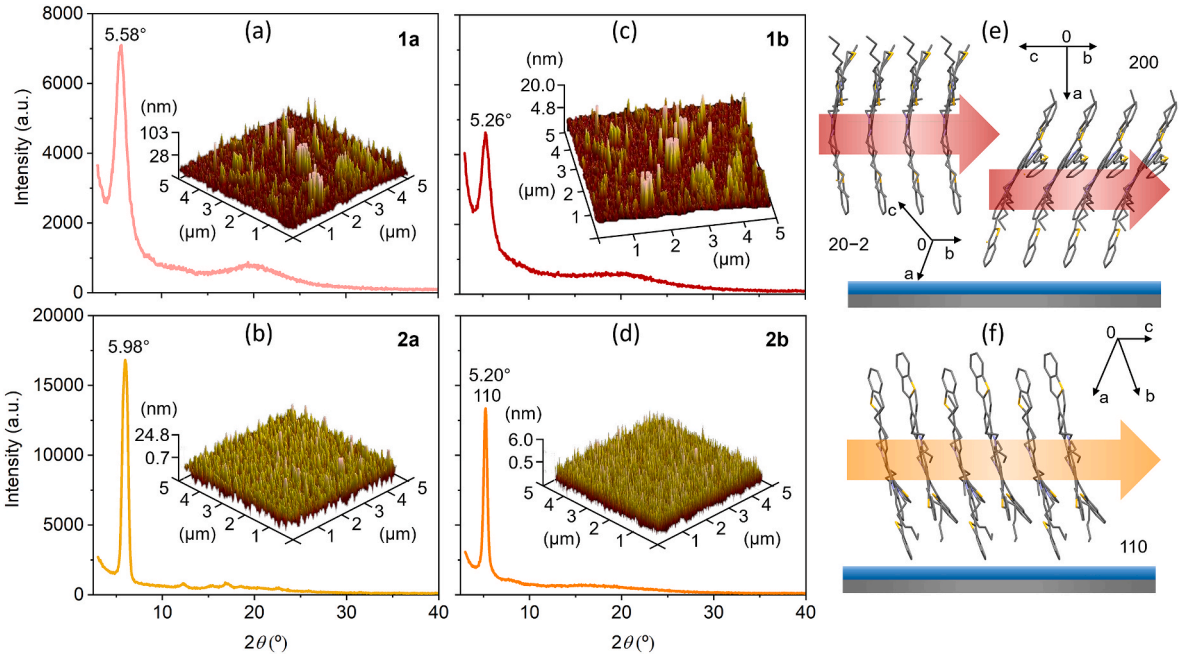

Fig. 6. GIXRD patterns of vacuum-evaporated thin-film of: a) **1a**, b) **2a**, c) **1b** and d) **2b** over OTS-treated Si/SiO_2 substrates. The inset images show the morphology of the thin-films, obtained by means of AFM. The proposed orientation over the OTS-treated Si/SiO_2 substrates based on the single-crystal structures and the main diffraction peaks is depicted in e) for **1b** and f) for **2b**.

aromatic scaffolds bonded to the main triindole nucleus also influence the performance of the materials. The incorporation of the two-ringed benzothienyl moieties is more favorable in terms of μ_h, but at the cost of displacing the V_{th} towards slightly negative values. In fact, the effect of the *meta*-substitution over triindole is more beneficial than any of the functionalizations proposed heretofore, namely the nature of the substituents [26] and the length of the *N*-alkyl chains [27]. Not only that, but the functionalization with *meta*-benzothienyl scaffolds in **2b** keeps pace with the outstanding performance of the bare trihexylated-triindole nucleus in OTS-treated OTFTs [16,18], pointing out the relevance of well-targeted structural modifications.

Keeping in mind the excellent air-stability previously observed for the triindole core, the performance of representative devices was measured periodically (Fig. 5). As observed, all derivatives exhibited an abrupt increase of the μ_h within the first two days after fabrication, which is associated to an early doping via oxidation that smooths hole injection and transport. Notably, they preserved their semiconductor properties thereafter, with small fluctuation of the μ_h under aerated conditions throughout the analyzed period of 5 months. The OTFT characteristics of a representative **2b**-based device 170 days after its fabrication are represented in Fig. S8.

3.5. Solid-state characterization

The reasons of the outperformance of the *meta*-substituted triindoles have been sought in the nanoscale. Hence, the disposition of the materials within the thin films deposited over OTS-treated Si/SiO_2 substrates was explored by means of grazing incident X-ray diffraction. All GIXRD patterns (Fig. 6) display a single diffraction peak, which could suggest a preferred orientation within the layer. Interestingly, the GIXRD patterns of **2a**,**b** exhibit sharper diffraction peaks with considerably higher intensities than those of their analogs **1a**,**b**, which is indicative of a higher degree of order in solid state.

The molecular disposition of compounds **1b** and **2b** within the films can be elucidated by combining the powder pattern simulations from the single crystal structures with their corresponding GIXRD data. As previously reported by our group, the diffraction peak corresponding to **1b** at $2\theta = 5.26°$ could be assigned to two different orientations, both of them placing the π-stacking direction (b-axis) parallel to the substrate (Fig. 6e). In the case of **2b**, the peak at $2\theta = 5.20°$ could be ascribed to the reflection 110, implying that the plane (110) is parallel to the OTS-treated Si/SiO_2 surface. Consequently, **2b** also organizes with the π–π stacking direction (c-axis) parallel to the substrate (Fig. 6f). Therefore, both compounds adopt appropriate molecular orientations that are prone to favoring the carrier transportation in the OTFTs. However, the higher degree of crystallinity detected for the *meta*-substituted derivatives along with the more optimum and well-orientated β-type packing with closer π-π distances of **2b** go in accordance with their better characteristics as semiconductors. The morphology of the films, analyzed by means of atomic force microscopy, also support this fact with more uniformity and less rugosity than those corresponding to the *para*-substituted counterparts. Indeed, a lower-quality interface between the semiconductor and the electrodes could also contribute to the underperformance of compounds **1a**,**b**. The AFM images are shown as insets in Fig. 6a–d.

4. Conclusions

The synthetic procedure was successful in providing *para*- and *meta*-substituted triindole derivatives. The anchoring position of the sulfurated scaffolds was actually determinant on the tailoring of all properties of the triindole core. In fact, the transition from the *para*- (**1a**,**b**) to the *meta*-functionalized structures (**2a**,**b**) implied several improvements: first, the melting temperatures substantially raised, inducing a more crystalline arrangement; second, the quantum yields in solution similarly raised, peaking at a notable value of 0.49 in CH_2Cl_2 for compound **2b**; third, the π-conjugation between the triindole core and the sulfurated moieties also increased, as determined by the decrease of the energy band gaps; fourth, the resulting HOMO energy levels are closer to the gold work function, i.e. are more adequate for hole injection, and still sufficiently low-lying to grant air-stability. To a lesser extent, these enhancements also occur with the inclusion of the more π-extended 2-benzothienyl scaffolds with respect to their 2-thienyl counterparts. In terms of hole transport properties, the change from *para*- to *meta*-

functionalization implies approximately a 5-fold increase. Indeed, the inclusion of 2-benzothienyl moieties in *meta* (**2b**) provided the highest value, i.e. 2×10^{-3} cm^2 V^{-1} s^{-1}, which stands with that of the unsubstituted counterpart in OTS-treated devices. The convenient β-type packing and shorter π-π distances exhibited by **2b** along with the higher degree of order and better morphology of the *meta* derivatives go in accordance with their superiority as semiconductors with respect to the *para* analogs. The prominent air-stability of the triindole core is preserved regardless of the functionalization motif, with a shelf lifetime that exceeds the 5 months with small fluctuation of the hole mobility.

5. Associated content

The following files are available free of charge. Synthesis and characterization, characteristics and ORTEP of the single crystal of derivative **2b**, optical properties, thermal properties, cyclic voltammetries, photoemission spectra, output curves of the OTFTs and OTFT characteristics of **2b** after 170 days.

Funding sources

This research was funded by the *Ministerio de Economía, Indústria y Competitividad* (grant number FUNMAT-PGC2018-095477-B-I00).

CRediT authorship contribution statement

Alba Cuadrado: Writing – original draft, Investigation. **Roger Bujaldón:** Writing – original draft, Investigation. **Clara Fabregat:** Investigation. **Joaquim Puigdollers:** Supervision. **Dolores Velasco:** Writing – review & editing, Conceptualization.

Declaration of competing interest

The authors declare that they have no known competing financial interests or personal relationships that could have appeared to influence the work reported in this paper.

Data availability

Data will be made available on request.

Acknowledgment

A.C., R.B. and C.F. are grateful for the grant FI AGAUR from Generalitat de Catalunya. The authors want to acknowledge Juozas V. Grazulevicius and Dmytro Volyniuk for their support with the measures of the IP and quantum yields in the solid state. Also, they thank Mercè Font and Josep M. Bassas of the X-Ray Diffraction Unit of the CCiTUB for their assistance with the measurements and interpretation of the single crystals and the GIXRD, respectively, and the staff of the Nanometric Techniques Unit for the AFM measures.

Appendix A. Supplementary data

Supplementary data to this article can be found online at https://doi.org/10.1016/j.orgel.2024.107020.

References

[1] F. Wu, Y. Liu, J. Zhang, S. Duan, D. Ji, H. Yang, Recent advances in high-mobility and high-stretchability organic field-effect transistors: from materials, devices to applications, Small Methods 5 (2021) 2100676, https://doi.org/10.1002/smtd.202100676.

[2] X. Jia, C. Fuentes-Hernandez, C.-Y. Wang, Y. Park, B. Kippelen, Stable organic thin-film transistors, Sci. Adv. 4 (2018) eaao1705, https://doi.org/10.1126/sciadv.aao1705.

[3] C.Y. Zheng, T. Tong, Y.M. Hu, Y.M. Gu, H.R. Wu, D.Q. Wu, H. Meng, M.D. Yi, J. Ma, D.Q. Gao, W. Huang, Charge-storage aromatic amino compounds for nonvolatile organic transistor memory devices, Small 14 (2018) 1800756, https://doi.org/10.1002/smll.201800756.

[4] C. Hayasaka, S. Nagano, K. Nakano, Synthesis of π-extended oxacenes and their application to organic field-effect transistors, Org. Electron. 100 (2022) 106335, https://doi.org/10.1016/j.orgel.2021.106335.

[5] M.N. Khatun, A. Dey, N. Meher, P.K. Iyer, Long alkyl chain induced OFET characteristic with low threshold voltage in an n-type perylene monoimide semiconductor, ACS Appl. Electron. Mater. 3 (2021) 3575–3587, https://doi.org/10.1021/acsaelm.1c00483.

[6] N. Onojima, N. Akiyama, Y. Mori, T. Sugai, S. Obata, Small molecule/polymer blends prepared by environmentally-friendly process for mechanically-stable flexible organic field-effect transistors, Org. Electron. 78 (2020) 105597, https://doi.org/10.1016/j.orgel.2019.105597.

[7] H. Bronstein, C.B. Nielsen, B.C. Schroeder, I. McCulloch, The role of chemical design in the performance of organic semiconductors, Nat. Rev. Chem 4 (2020) 66–77, https://doi.org/10.1038/s41570-019-0152-9.

[8] H. Zhu, E.S. Shin, A. Liu, D. Ji, Y. Xu, Y.Y. Noh, Printable semiconductors for backplane TFTs of flexible OLED displays, Adv. Funct. Mater. 30 (2019) 1904588, https://doi.org/10.1002/adfm.201904588.

[9] H. Peng, X. He, H. Jiang, Greater than 10 cm^2 V^{-1} s^{-1}: a breakthrough of organic semiconductors for field-effect transistors, InfoMat 3 (2021) 613–630, https://doi.org/10.1002/inf2.12188.

[10] H. Jiang, S. Zhu, Z. Cui, Z. Li, Y. Liang, J. Zhu, P. Hu, H.-L. Zhang, W. Hu, High-performance five-ring-fused organic semiconductors for field-effect transistors, Chem. Soc. Rev. 51 (2022) 3071–3122, https://doi.org/10.1039/D1CS01136G.

[11] Z. He, K. Asare-Yeboah, Z. Zhang, S. Bi, Manipulate organic crystal morphology and charge transport, Org. Electron. 103 (2022) 106448, https://doi.org/10.1016/j.orgel.2022.106448.

[12] M. Nikolka, I. Nasrallah, B. Rose, M.K. Ravva, K. Broch, A. Sadhanala, D. Harkin, J. Charmet, M. Hurhangee, A. Brown, S. Illig, P. Too, J. Jongman, I. McCulloch, J.-L. Bredas, H. Sirringhaus, High operational and environmental stability of high-mobility conjugated polymer field-effect transistors through the use of molecular additives, Nat. Mater. 16 (2017) 356–362, https://doi.org/10.1038/nmat4785.

[13] X. Chen, Z. Wang, J. Qi, Y. Hu, Y. Huang, S. Sun, Y. Sun, W. Gong, L. Luo, L. Zhang, H. Du, X. Hu, C. Han, J. Li, D. Ji, L. Li, W. Hu, Balancing the film strain of organic semiconductors for ultrastable organic transistors with a five-year lifetime, Nat. Commun. 13 (2022) 1480, https://doi.org/10.1038/s41467-022-29221-8.

[14] R. Bujaldón, A. Vilche, J. Puigdollers, C. Puigjaner, X. Alcobé, D. Velasco, Insight into the diindolo[3,2-*b*:2′,3′-*h*]carbazole core as an air-stable semiconductor for OTFTs, ACS Appl. Electron. Mater. 5 (2023) 3675–3684, https://doi.org/10.1021/acsaelm.3c00412.

[15] E.M. García-Frutos, E. Gutierrez-Puebla, M.A. Monge, R. Ramírez, P. de Andrés, A. de Andrés, R. Ramírez, B. Gómez-Lor, Crystal structure and charge-transport properties of *N*-trimethyltriindole: novel p-type organic semiconductor single crystals, Org. Electron. 10 (2009) 643–652, https://doi.org/10.1016/j.orgel.2009.02.016.

[16] C. Ruiz, I. Arrechea-Marcos, A. Benito-Hernández, E. Gutierrez-Puebla, M. A. Monge, J.T. López Navarrete, M.C. Ruiz Delgado, R. Ponce Ortiz, Berta Gómez-Lor, Solution-processed *N*-trialkylated triindoles for organic field effect transistors, J. Mater. Chem. C 6 (2018) 50–56, https://doi.org/10.1039/c7tc03866f.

[17] M. Reig, J. Puigdollers, D. Velasco, Molecular order of air-stable p-type organic thin-film transistors by tuning the extension of the π-conjugated core: the cases of indolo[3,2-*b*]carbazole and triindole semiconductors, J. Mater. Chem. C 3 (2015) 506–513, https://doi.org/10.1039/C4TC01692K.

[18] M. Reig, G. Bagdziunas, A. Ramanavicius, J. Puigdollers, D. Velasco, Interface engineering and solid-state organization for triindole-based p-type organic thin-film transistors, Phys. Chem. Chem. Phys. 20 (2018) 17889–17898, https://doi.org/10.1039/C8CP02963F.

[19] S. Mula, T. Han, T. Heiser, P. Lévêque, N. Leclerc, A.P. Srivastava, A. Ruiz-Carretero, G. Ulrich, Hydrogen bonding as a supramolecular tool for robust OFET devices, Chem. Eur J. 25 (2019) 8304–8312, https://doi.org/10.1002/chem.201900689.

[20] Y.-C. Hu, Z.-L. Lin, T.-C. Huang, J.-W. Lee, W.-C. Wei, T.-Y. Ko, C.-Y. Lo, D.-G. Chen, P.-T. Chou, W.-Y. Hung, K.-T. Wong, New exciplex systems composed of triazatruxene donors and *N*-heteroarene-cored acceptors, Mater. Chem. Front. 4 (2020) 2029–2039, https://doi.org/10.1039/D0QM00188K.

[21] Y. Chen, S. Wang, X. Wu, Y. Xu, H. Li, Y. Liu, H. Tong, L. Wang, Triazatruxene-based small molecules with thermally activated delayed fluorescence, aggregation-induced emission and mechanochromic luminescence properties for solution-processable nondoped OLEDs, J. Mater. Chem. C 6 (2018) 12503–12508, https://doi.org/10.1039/C8TC04721A.

[22] T. Han, I. Bulut, S. Méry, B. Heinrich, P. Lévêque, N. Leclerc, T. Heiser, Improved structural order by side-chain engineering of organic small molecules for photovoltaic applications, J. Mater. Chem. C 5 (2017) 10794–10800, https://doi.org/10.1039/c7tc03155f.

[23] K. Rakstys, S. Paek, P. Gao, P. Gratia, T. Marszalek, G. Grancini, K.T. Cho, K. Genevicius, V. Jankauskas, W. Pisulab, M.K. Nazeeruddin, Molecular engineering of face-on oriented dopant-free hole transporting material for perovskite solar cells with 19% PCE, J. Mater. Chem. A 5 (2017) 7811–7815, https://doi.org/10.1039/c7ta01718a.

[24] A. Benito-Hernández, U.K. Pandey, E. Cavero, R. Termine, E.M. García-Frutos, J. L. Serrano, A. Golemme, B. Gómez-Lor, High hole mobility in triindole-based columnar phases: removing the bottleneck of homogeneous macroscopic orientation, Chem. Mater. 25 (2013) 117–121, https://doi.org/10.1021/cm3033548.

[25] C. Ruiz, U.K. Pandey, R. Termine, E.M. García-Frutos, G. López-Espejo, R. Ponce Ortiz, W. Huang, T.J. Marks, A. Facchetti, M.C. Ruiz Delgado, A. Golemme, B. Gómez-Lor, Mobility versus alignment of a semiconducting π-extended discotic liquid-crystalline triindole, ACS Appl. Mater. Interfaces 8 (2016) 26964–26971, https://doi.org/10.1021/acsami.6b06241.

[26] A. Cuadrado, J. Cuesta, J. Puigdollers, D. Velasco, Air stable organic semiconductors based on diindolo[3,2-*a*:3′,2′-*c*]carbazole, Org. Electron. 62 (2018) 35–42, https://doi.org/10.1016/j.orgel.2018.07.004.

[27] R. Bujaldón, A. Cuadrado, D. Volyniuk, J.V. Grazulevicius, J. Puigdollers, D. Velasco, Role of the alkylation patterning in the performance of OTFTs: the case of thiophene-functionalized triindoles, Coatings 13 (2023) 896, https://doi.org/10.3390/coatings13050896.

[28] K. Takimiya, S. Shinamura, I. Osaka, E. Miyazaki, Thienoacene-based organic semiconductors, Adv. Mater. 23 (2011) 4347–4370, https://doi.org/10.1002/adma.201102007.

[29] J.W. Borchert, B. Peng, F. Letzkus, J.N. Burghartz, P.K.L. Chan, K. Zojer, S. Ludwigs, H. Klauk, Small contact resistance and high-frequency operation of flexible low-voltage inverted coplanar organic transistors, Nat. Commun. 10 (2019) 1119, https://doi.org/10.1038/s41467-019-09119-8.

[30] R. Bujaldón, J. Puigdollers, D. Velasco, Towards the bisbenzothienocarbazole core: a route of sulfurated carbazole derivatives with assorted optoelectronic properties and applications, Materials 14 (2021) 3487, https://doi.org/10.3390/ma14133487.

[31] M. Sugiyama, J. Jancke, T. Uemura, M. Kondo, Y. Inoue, N. Namba, T. Araki, T. Fukushima, T. Sekitani, Mobility enhancement of DNTT and BTBT derivative organic thin-film transistors by triptycene molecule modification, Org. Electron. 96 (2021) 106219, https://doi.org/10.1016/j.orgel.2021.106219.

[32] C.M. Cardona, W. Li, A.E. Kaifer, D. Stockdale, G.C. Bazan, Electrochemical considerations for determining Absolute frontier orbital energy levels of conjugated polymers for solar cell applications, Adv. Mater. 23 (2011) 2367–2371, https://doi.org/10.1002/adma.201004554.

[33] E. Miyamoto, Y. Yamaguchi, M. Yokoyama, Ionization potential of organic pigment film by atmospheric photoelectron emission analysis, Electrophotography 28 (1989) 364–370.

[34] A. Ghalgaoui, R. Shimizu, S. Hosseinpour, R. Álvarez-Asencio, C. McKee, C. M. Johnson, M.W. Rutland, Monolayer study by VSFS: in situ response to compression and shear in a contact, Langmuir 30 (2014) 3075–3085, https://doi.org/10.1021/la4042474.

[35] C. Crestini, R. Saladino, A new efficient and mild synthesis of 2-sxindoles by one-pot wolff-kishner like reduction of isatin derivatives, Synth. Commun. 24 (1994) 2835, https://doi.org/10.1080/00397919408010603.

[36] N. Miyaura, A. Suzuki, Palladium-catalyzed cross-coupling reactions of organoboron compounds, Chem. Rev. 95 (1995) 2457–2483, https://doi.org/10.1021/cr00039a007.

[37] G.R. Desiraju, A. Gavezzotti, Crystal structures of polynuclear aromatic hydrocarbons. Classification, rationalization and prediction from molecular structure, Acta Crystallogr. 45 (1989) 473–482, https://doi.org/10.1107/S0108768189003794.

[38] J.E. Campbell, J. Yang, G.M. Day, Predicted energy–structure–function maps for the evaluation of small molecule organic semiconductors, J. Mater. Chem. C 5 (2017) 7574–7584, https://doi.org/10.1039/c7tc02553j.

[39] M. Mas-Torrent, C. Rovira, Role of molecular order and solid-state structure in organic field-effect transistors, Chem. Rev. 111 (2011) 4833–4856, https://doi.org/10.1021/cr100142w.

[40] Z.-F. Yao, J.-Y. Wang, J. Pei, Control of π–π stacking via crystal engineering in organic conjugated small molecule crystals, Cryst. Growth Des. 18 (2018) 7–15, https://doi.org/10.1021/acs.cgd.7b01385.

[41] H.H. Choi, K. Cho, C.D. Frisbie, H. Sirringhaus, V. Podzorov, Critical assessment of charge mobility extraction in FETs, Nat. Mater. 17 (2018) 2–7, https://doi.org/10.1038/nmat5035.

[42] I. McCulloch, A. Salleo, M. Chabinyc, Avoid the kinks when measuring mobility, Science 352 (2016) 1521–1522, https://doi.org/10.1126/science.aaf9062.